Electronic Supplementary Material (ESI) for Dalton Transactions.
This journal is © The Royal Society of Chemistry 2024

Electronic Supporting Information

Coordination-triggered redox activity of early and late lanthanide calix[4]arene complexes

Yushu Jiao,[a] Sergio Sanz,*[b] Lucie Koláčná,[c] Jan van Leusen,[a] Natalya V. Izarova,[a] Sidra Sarwar,[a] Jiří Ludvík*[c] and Paul Kögerler*[a,b]

a. Institute of Inorganic Chemistry, RWTH Aachen University, 52056 Aachen, Germany.
b. Peter Grünberg Institute 6, Forschungszentrum Jülich, 52425 Jülich, Germany.
c. J. Heyrovský Institute of Physical Chemistry AS CR, Dept. of Molecular Electrochemistry and Catalysis, Dolejškova 2155/3, 182 23 Prague 8, Czech Republic.

Contents

I. Synthesis

I.1. Instrumentation

Microcrystalline samples of **1 – 4** used for EA, ESI-HRMS, UV-Vis spectra, IR spectra, PXRD, TGA, magnetic, and electrochemical measurements are represented by the composition $(N(n\text{Bu})_4)[Ln^{III}L(acac)_2]\cdot CH_3CN$, whereas the rapid loss of crystal solvent (MeCN) content observed for compounds **5** and **6**, which is complete after ca. 3 h upon removal from the reaction solution under ambient conditions, requires using the solvent-free formula $(N(n\text{Bu})_4)_2[Ln^{III}L\{Mo_5O_{13}(OMe)_4(NO)\}]$ for analytical purposes. Elemental analyses were obtained from the Institute of Organic Chemistry, RWTH Aachen University (Elementar VarioEL). Electrospray mass spectra (ESI-HRMS) were performed using a MAT 95-maXis II mass spectrometer. UV-Vis spectra were measured in CH_3CN solutions on a Shimadzu UV–2600 spectrophotometer (10 mm quartz glass cuvettes). IR spectra were collected on a Bruker VERTEX 70 FT-IR spectrometer coupled with a RAM II FT-Raman module. TGA measurements were performed on a Mettler Toledo SDTA 851 in an air atmosphere. Powder X-ray diffraction was recorded at room temperature on a STOE StadiP diffractometer.

Single-crystal diffraction data for **1 – 6** were collected on a STOE STADIVARI diffractometer with MoKα radiation (λ = 0.71073 Å) at 100 K. The crystals were mounted on a Hampton cryoloop with Paratone-N oil to prevent water loss. Absorption corrections were applied numerically based on a multifaceted crystal model using either STOE X-Red32 software[1] with the following scaling of reflection intensities or performed within STOE LANA.[2] The SHELXTL software package[3] was applied to solve and refine the structures.

Magnetic properties were measured by a Quantum Design MPMS–5XL SQUID magnetometer for direct current (dc) and alternating current (ac) modes measurements. Microcrystalline samples of **1 – 6** were separately compacted and immobilized into cylindrical PTFE sample holders. Experimental dc data were recorded at 0.1 T and 1.0 T in the temperature range 2.0–290 K, and at 2.0 K in the field range 0.1–5.0 T. Experimental ac data were collected at various static bias fields between 0 and 1000 Oe in the temperature range 2.0–50 K and frequency range 3–1000 Hz using an amplitude of B_{ac} = 3 G. However, relevant out-of-phase signals were only detected for **4** and **6** in this parameter range. All data were corrected for the diamagnetic contributions of the sample holders and the complex. For **5** and **6**, the data of $(N(n\text{Bu})_4)_2[Y^{III}L\{Mo_5O_{13}(OMe)_4(NO)\}]$ was used as diamagnetic reference ($\chi_{m,dia}$ / 10^{-4} cm^3 mol^{-1} = –6.96 (**1**), –6.51 (**2**), –6.61 (**3**), –6.83 (**4**), –9.03 (**5**), –9.24 (**6**)).

For electrochemical studies, one steady state (RDE voltammetry; 10 mV s^{-1}, 500/1000/1500 rpm) and one dynamic method (CV, scan rate 50–1000 mV s^{-1}) were used. To check the role of solvent and to exclude the electrode material assistance or surface catalysis, electrochemical experiments were performed in three aprotic solvents: dimethylformamide (DMF), acetonitrile (AN), and tetrahydrofuran (THF) and on three working electrode materials: glassy carbon (GC) stationary/rotating disk ∅ 3 mm, platinum, and hanging mercury drop. 0.1 M Tetrabutylammonium hexafluorophosphate ($N(n\text{Bu})_4PF_6$) served as the supporting electrolyte. In an undivided electrochemical cell, aqueous SCE separated from the measured solution by an aprotic salt bridge and Pt-sheet was used as a reference and auxiliary electrodes, respectively.

10 mL of the studied solution (conc. 0.5–1 x 10^{-3} mol L^{-1}) was fluxed with Argon before the measurement.

I.2. ESI-HRMS, EA, IR, and UV-Vis details

1 (N(*n*Bu)$_4$)[Pr^{III}L(acac)$_2$]·CH$_3$CN

ESI-HRMS *m*/*z*: found 1013.4228 [M – N(*n*Bu$_4$)]$^-$ (100% relative abundance), calculated for [$C_{56}H_{72}O_8Pr$]$^-$ 1013.4309. M stands for (N(*n*Bu)$_4$)[Pr^{III}L(acac)$_2$].
Elemental analysis (%) calculated for ($C_{74}H_{111}N_2O_8Pr$) {(N(*n*Bu)$_4$)[Pr^{III}L(acac)$_2$]·CH$_3$CN}: C, 68.50; H, 8.62; N, 2.16. Found C, 68.45; H, 8.56; N, 2.16.
IR (cm^{-1}): 2960 (s), 2900 (m), 2875 (m), 1591 (s), 1508 (s), 1481(vs), 1409 (m), 1342 (m), 1330 (m), 1247 (w), 1211 (w), 1168 (w), 1124 (w), 1095 (w), 1006 (m), 910 (w), 871 (w), 838 (w), 794 (w), 757 (w), 719 (w), 653 (w), 528 (w), 497 (w).
UV-Vis, CH$_3$CN, λ / nm (ε / 10^4 M^{-1} cm^{-1}): 250 (3.54) and 288 (3.87).

2 (N(*n*Bu)$_4$)$_2$[Nd^{III}L(acac)$_2$]·CH$_3$CN

ESI-HRMS *m*/*z*: found 1016.4264 [M – N(*n*Bu$_4$)]$^-$ (100% relative abundance), calculated for [$C_{56}H_{72}O_8Nd$]$^-$ 1013.4348. M stands for (N(*n*Bu)$_4$)[Nd^{III}L(acac)$_2$].
Elemental analysis (%) calculated for ($C_{74}H_{111}N_2O_8Nd$) {(N(*n*Bu)$_4$)[Nd^{III}L(acac)$_2$]·CH$_3$CN}: C, 68.32; H, 8.60; N, 2.15. Found C, 68.30; H, 8.57; N, 2.11.
IR (cm^{-1}): 2961 (s), 2898 (m), 2874 (m), 1588 (s), 1506 (s), 1479 (vs), 1406 (m), 1342 (m), 1330 (m), 1249 (w), 1207 (w), 1168 (w), 1124 (w), 1094 (w), 1004 (m), 909 (w), 871 (w), 838 (w), 794 (w), 756 (w), 708 (w), 652 (w), 527 (w), 496 (w).
UV-Vis, CH$_3$CN, λ / nm (ε / 10^4 M^{-1} cm^{-1}): 250 (3.65) and 288 (4.14).

3 (N(*n*Bu)$_4$)[Ho^{III}L(acac)$_2$]·CH$_3$CN

ESI-HRMS *m*/*z*: found 1037.4491 [M – N(*n*Bu$_4$)]$^-$ (100% relative abundance), calculated for [$C_{56}H_{72}O_8Ho$]$^-$ 1037.4536. M stands for (N(*n*Bu)$_4$)[Ho^{III}L(acac)$_2$].
Elemental analysis (%) calculated for ($C_{74}H_{111}N_2O_8Ho$) {(N(*n*Bu)$_4$)[Ho^{III}L(acac)$_2$]·CH$_3$CN}: C, 67.25; H, 8.47; N, 2.12. Found C, 67.02; H, 8.56; N, 2.11.
IR (cm^{-1}): 2962 (s), 2902 (m), 2875 (m), 1596 (s), 1510 (s), 1481(vs), 1411 (m), 1348 (m), 1334 (m), 1253 (w), 1211 (w), 1170 (w), 1124 (w), 1095 (w), 1006 (m), 910 (w), 871 (w), 840 (w), 792 (w), 755 (w), 719 (w), 653 (w), 528 (w), 495 (w).
UV-Vis, CH$_3$CN, λ / nm (ε / 10^4 M^{-1} cm^{-1}): 258 (3.45) and 285 (4.19).

4 (N(*n*Bu)$_4$)$_2$[Er^{III}L(acac)$_2$]·CH$_3$CN

ESI-HRMS *m*/*z*: found 1040.4540 [M – N(*n*Bu$_4$)]$^-$ (100% relative abundance), calculated for [$C_{56}H_{72}O_8Er$]$^-$ 1040.4572. M stands for (N(*n*Bu)$_4$)[Er^{III}L(acac)$_2$].
Elemental analysis (%) calculated for ($C_{74}H_{111}N_2O_8Er$) {(N(*n*Bu)$_4$)[Er^{III}L(acac)$_2$]·CH$_3$CN}: C, 67.13; H, 8.45; N, 2.12. Found C, 67.08; H, 8.21; N, 2.18.
IR (cm^{-1}): 2961 (s), 2900 (m), 2874 (m), 1593 (s), 1508 (s), 1479 (vs), 1409 (m), 1347 (m), 1333 (m), 1254 (w), 1206 (w), 1168 (w), 1127 (w), 1095 (w), 1005 (m), 911 (w), 872 (w), 839 (w), 794 (w), 756 (w), 711 (w), 653 (w), 527 (w), 497 (w).
UV-Vis, CH$_3$CN, λ / nm (ε / 10^4 M^{-1} cm^{-1}): 258 (3.64) and 282 (3.90).

5 $(N(nBu)_4)_2[Nd^{III}L\{Mo_5O_{13}(OMe)_4(NO)\}]\cdot CH_2Cl_2$

ESI-HRMS *m*/*z*: found 830.4362[M – 2 $N(nBu)_4]^{2-}$ (6.15% relative abundance), calculated for $[C_{50}H_{70}NO_{22}Mo_5Nd]^{2-}$ 830.4408; *m*/*z*: found 1904.1562 [M – $N(nBu)_4]^{1-}$ (100% relative abundance), calculated for $[C_{66}H_{106}N_2O_{22}Mo_5Nd]^{1-}$ 1904.1665. M stands for $(N(nBu)_4)_2[Nd^{III}L\{Mo_5O_{13}(OMe)_4(NO)\}]$.
Elemental analysis (%) calculated for $(C_{82}H_{142}N_3O_{22}Mo_5Nd)$ $(N(nBu)_4)_2[Nd^{III}L\{Mo_5O_{13}(OMe)_4(NO)\}]$: C, 45.89; H, 6.67; N, 1.96. Found C, 45.98; H, 6.860; N, 1.93.
IR (cm^{-1}): 2958 (m), 2913 (w), 2873 (w), 2811 (w), 1623 (m), 1480 (m), 1430 (m), 1390 (w), 1380 (w), 1359 (w), 1328 (m), 1309 (m), 1274 (w), 1211 (w), 1170 (w), 1122 (w), 1097 (w), 1066 (w), 1037 (m), 1010 (m), 927 (s), 888 (s), 861 (vs), 836 (s), 815 (m), 792 (m), 773 (m), 736 (w), 678 (vs), 630 (s), 563 (s), 526 (m), 499 (m), 482 (m), 431 (s), 399 (m), 374 (s).
UV-Vis, CH_3CN, λ / nm (ε / 10^4 M^{-1} cm^{-1}): 246 (1.21) and 306 (4.49).

6 $(N(nBu)_4)_2[Er^{III}L\{Mo_5O_{13}(OMe)_4(NO)\}]\cdot CH_2Cl_2$

ESI–HRMS *m*/*z*: found 841.9478[M – 2 $N(nBu)_4]^{2-}$ (100% relative abundance), calculated for $[C_{50}H_{70}NO_{22}Mo_5Er]^{2-}$ 841.9515; *m*/*z*: found 1926.1787 [M – $N(nBu)_4]^{1-}$ (45.78% relative abundance), calculated for $[C_{66}H_{106}N_2O_{22}Mo_5Er]^{1-}$ 1926.1875. M stands for $(N(nBu)_4)_2[Er^{III}L\{Mo_5O_{13}(OMe)_4(NO)\}]$.
Elemental analysis (%) calculated for $(C_{82}H_{142}N_3O_{22}Mo_5Er)$ $(N(nBu)_4)_2[Er^{III}L\{Mo_5O_{13}(OMe)_4(NO)\}]$: C, 45.41; H, 6.60; N, 1.94. Found C, 45.86; H, 6.847; N, 2.02.
IR (cm^{-1}): 2958 (m), 2913 (w), 2873 (w), 2811 (w), 1621 (m), 1479 (m), 1430 (m), 1390 (w), 1380 (w), 1359 (w), 1334 (m), 1315 (m), 1276 (w), 1212 (w), 1170 (w), 1124 (w), 1097 (w), 1064 (w), 1039 (m), 1012 (m), 927 (s), 888 (s), 863 (vs), 838 (s), 815 (m), 790 (m), 775 (m), 736 (w), 680 (vs), 630 (s), 565 (s), 530 (m), 501 (m), 480 (m), 435 (s), 399 (m), 379 (s).
UV-Vis, CH_3CN, λ / nm (ε / 10^4 M^{-1} cm^{-1}): 246 (1.33) and 306 (4.26).

II. X-ray crystallography

II.1. Single-crystal X-ray diffraction

The structures of **1 – 6** were solved by direct methods and refined by full-matrix least-squares method against $|F|^2$ with anisotropic thermal parameters for all non-hydrogen atoms (Ln, Mo, O, N, and C). ISOR restrictions had to be applied for some C atoms of the isopropyl groups of TBC[4] (**1**, **2**, **4**, and **5**) and of terminal $-CH_2-CH_3$ groups of $N(nBu_4)^+$ countercations (**5**, **6**). The isopropyl groups in TBC[4] in **1 – 4** exhibit a rotational disorder and two possible positions were located for every CH_3 group in the isopropyl functions. Their site occupancy factors were refined using PART commands. One of the $-CH_2-CH_3$ groups of one of the $N(nBu_4)^+$ countercation in **6** was also disordered over two positions, those site occupancy factors were refined with the help of PART/EADP commands. N and bound C atoms of the co-crystallized acetonitrile molecule in the structures of **1 – 4** were disordered over two positions with 0.5 site occupancy factors. Hydrogen atoms of this acetonitrile molecule in all four structures (**1 – 4**) were not located. All the other hydrogen atoms in the six structures were placed in geometrically calculated positions

besides hydrogens of the CH− groups of acetylacetonate ligands in the structures of **3** and **4** which were located directly from the electron density.

Additional crystallographic data are summarized in Tables S1 (**1 – 4**) and S2 (**5**, **6**). Further details on the crystal structures investigation can be obtained, free of charge, on application to CCDC, 12 Union Road, Cambridge CB2 1EZ, UK: http://www.ccdc.cam.ac.uk/, e-mail: data_request@ccdc.cam.ac.uk, or fax: +441223 336033 upon quoting 2299497 (**1**), 2299498 (**2**), 2299499 (**3**), 2299500 (**4**), 2299501 (**5**) and 2299502 (**6**) numbers.

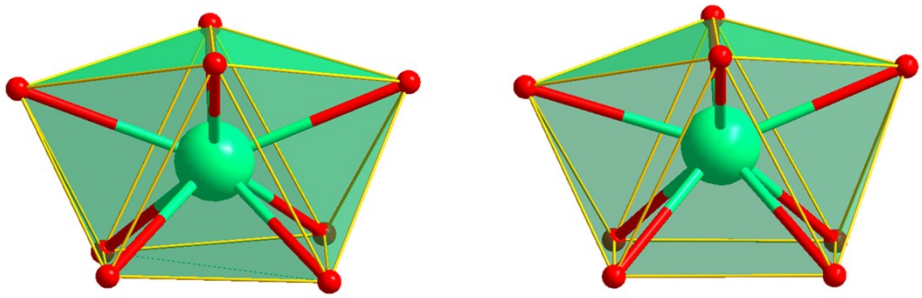

Fig. S1. The coordination geometry of the Er^{III} ions in **4** and **6**. The two Er^{III} ions are both octa-coordinated. For both **4** and **6**, continuous shape measure calculations using SHAPE 2.1[4] indicate that the coordination environments can be best described as (slightly distorted) bicapped trigonal prismatic (Johnson solid 50) with local C_{2v} symmetry.

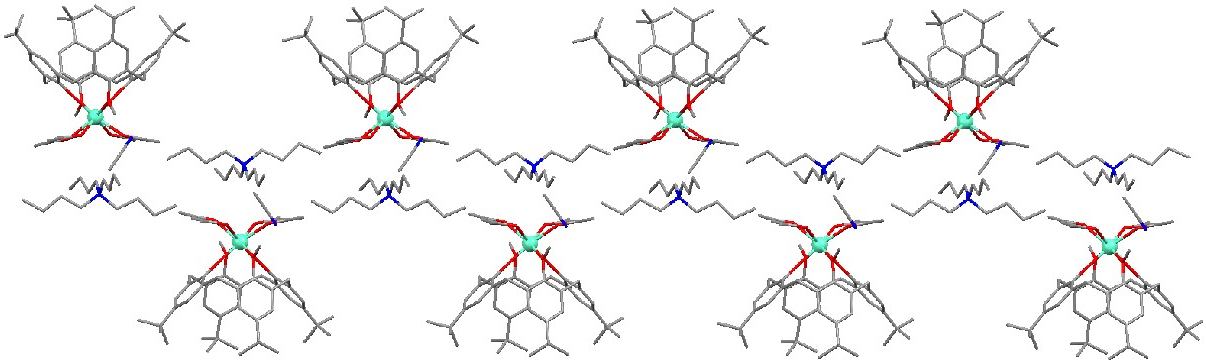

Fig. S2. Extended molecular structure of **4** with the Er^{III} ions highlighted as spheres. Color code: Er: green, O: red, N: blue, and C: gray. H atoms omitted for clarity.

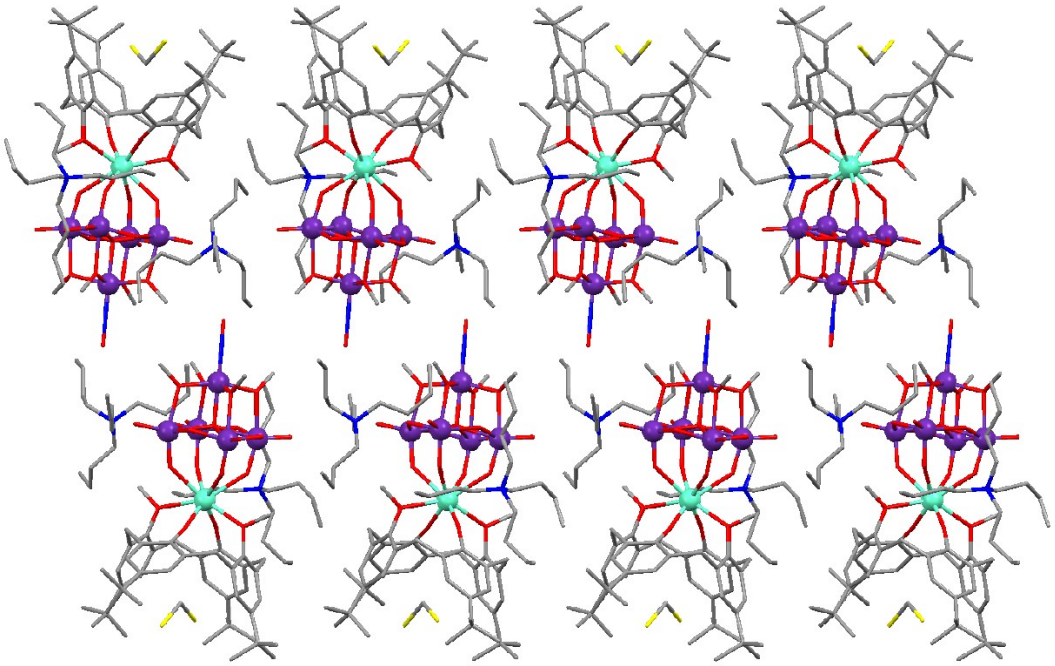

Fig. S3. Extended molecular structure of **6** with the Er and Mo atoms highlighted as spheres. CH_2Cl_2 molecules are located in the cavities of the L^{2-} ligand, and tetrabutylammonium cations crystallize in the interstitial space. Color code: Er: green, O: red, Cl: yellow, N: blue, Mo: purple, and C: gray. H atoms omitted for clarity.

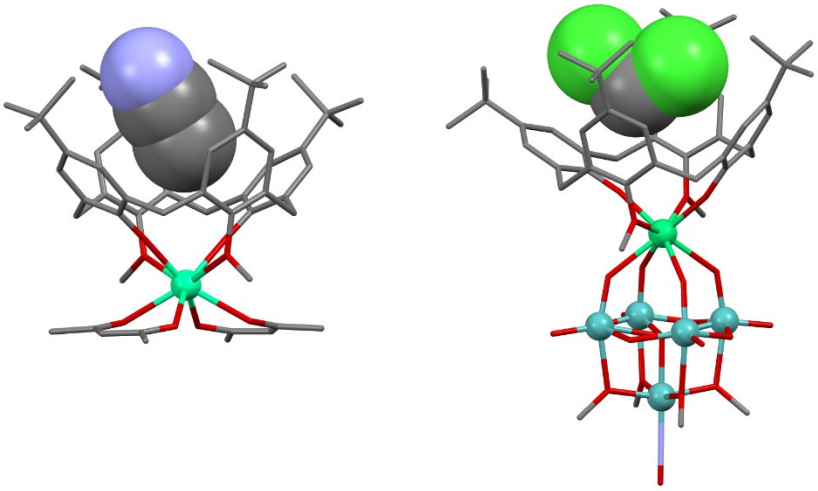

Fig. S4. The host-guest interactions of the calix[4]arene ligands and crystal solvent molecules in the solid-state structures of **4** (left, CH_3CN) and **6** (right, CH_2Cl_2). The packing effect of the molecules also contributes to the stability of the encapsulated molecules. Note that in calix[4]arene chemistry, CH_3CN is known to be easily encapsulated and stabilized. Given its linear shape, CH_3CN reaches deeper into the hydrophobic pocket of calix[4]arene where the hydrogen atoms interact with the aromatic phenoxide rings (see e.g. S. Sanz, K. Ferreira, R. D. McIntosh, S. J. Dalgarno, E. K. Brechin, *Chem. Commun.*, 2011, **47**, 9042–9044).

Table S1. Crystal data and structure refinement details for **1 – 4.**

Sample	**1**	**2**	**3**	**4**
Empirical formula	$C_{74}H_{111}N_2O_8Pr$	$C_{74}H_{111}N_2O_8Nd$	$C_{74}H_{111}N_2O_8Ho$	$C_{74}H_{111}N_2O_8Er$
Formula weight / g mol^{-1}	1297.55	1300.88	1321.57	1323.90
Crystal system	Monoclinic	Monoclinic	Monoclinic	Monoclinic
Space group	*C*2/*c*	*C*2/*c*	*C*2/*c*	*C*2/*c*
a / Å	23.746(5)	23.771(5)	23.831(5)	23.790(5)
b / Å	16.124(3)	16.145(3)	16.057(3)	16.055(3)
c / Å	21.064(4)	21.069(4)	21.071(4)	21.038(4)
β	120.16(3)°	120.26(3)°	120.42(3)°	120.40(3)°
Volume / Å^3	6973(3)	6984(3)	6953(3)	6931(3)
Z	4	4	4	4
D_{calc} / g cm^{-3}	1.236	1.237	1.263	1.269
Absorption coefficient / mm^{-1}	0.753	0.797	1.192	1.265
F (000)	2768	2772	2800	2804
Crystal size / mm^3	0.07 × 0.10 × 0.27	0.05 × 0.11 × 0.32	0.05 × 0.05 × 0.20	0.075 × 0.21 × 0.30
Theta range for data collection	2.11° – 25.02°	2.11° – 25.02°	2.11° – 25.02°	2.11° – 25.02°
Completeness to Θ_{max}	99.4 %	99.9 %	99.9 %	99.9 %
Index ranges	–28 < *h* < 28, –19 < *k* < 19, –20 < *l* < 25	–28 < *h* < 28, –19 < *k* < 18, –25 < *l* < 25	–28 < *h* < 28, –19 < *k* < 19, –25 < *l* < 25	–28 < *h* < 28, –19 < *k* < 15, –25 < *l* < 25
Reflections collected	36655	35449	36272	32953
Independent reflections	6124	6166	6136	6114
R_{int}	0.0755	0.1111	0.0626	0.0525
Observed ($I > 2\sigma(I)$)	4506	4033	5110	5309
Absorption correction	Gaussian integration			
T_{min} / T_{max}	0.8574 / 0.9017	0.6229 / 0.8726	0.5668 / 0.9832	0.3745 / 0.7697
Data / restraints / parameters	6124 / 72 / 450	6166 / 36 / 450	6136 / 0 / 454	6114 / 36 / 454
Goodness-of-fit on F^2	1.018	1.035	1.043	1.047
R_1, wR_2 ($I > 2\sigma(I)$)	R_1 = 0.0611, wR_2 = 0.1539	R_1 = 0.0697, wR_2 = 0.1722	R_1 = 0.0581, wR_2 = 0.1443	R_1 = 0.0579, wR_2 = 0.1454
R_1, wR_2 (all data)	R_1 = 0.0828, wR_2 = 0.1612	R_1 = 0.1083, wR_2 = 0.1848	R_1 = 0.0697, wR_2 = 0.1486	R_1 = 0.0657, wR_2 = 0.1487
Largest diff. peak and hole / e Å^{-3}	1.167 / –0.848	1.084 / –1.442	1.477 / –1.808	1.804 / –1.889

Table S2. Crystal data and structure refinement details for **5** and **6.**

Sample	**5**	**6**
Empirical formula	$C_{83}H_{144}Cl_2Mo_5N_3O_{22}Nd$	$C_{83}H_{144}Cl_2Mo_5N_3O_{22}Er$
Formula weight / g mol^{-1}	2230.84	2253.86
Crystal system	Monoclinic	Monoclinic
Space group	*C*2/*c*	*C*2/*c*
a / Å	67.598(14)	66.701(13)
b / Å	12.541(3)	12.581(3)
c / Å	23.425(5)	23.523(5)
β	103.49(3)°	103.25(3)°
Volume / Å^3	19311(7)	19213(7)
Z	8	8
D_{calc} / g cm^{-3}	1.535	1.558
Absorption coefficient / mm^{-1}	1.279	1.619
F (000)	9144	9208
Crystal size / mm^3	0.10 × 0.14 × 0.41	0.07 × 0.20 × 0.33
Theta range for data collection	2.29° – 25.02°	2.16° – 25.02°
Completeness to Θ_{max}	99.0 %	99.7 %
Index ranges	–78 < *h* < 80, –9 < *k* < 14, –27 < *l* < 27	–79 < *h* < 79, –14 < *k* < 14, –28 < *l* < 27
Reflections collected	87889	85513
Independent reflections	16875	16897
R_{int}	0.0553	0.0802
Observed ($I > 2\sigma(I)$)	13308	11966
Absorption correction	Gaussian integration	
T_{min} / T_{max}	0.4109 / 0.7013	0.6180 / 0.8846
Data / restraints / parameters	16875 / 30 / 1045	16897 / 48 / 1052
Goodness-of-fit on F^2	1.026	1.005
R_1, wR_2 ($I > 2\sigma(I)$)	R_1 = 0.0490, wR_2 = 0.1218	R_1 = 0.0660, wR_2 = 0.1692
R_1, wR_2 (all data)	R_1 = 0.0652, wR_2 = 0.1430	R_1 = 0.0898, wR_2 = 0.1833
Largest diff. peak and hole / e Å^{-3}	1.712 / –1.540	2.285 / –2.955

Table S3. Selected bond lengths for **1 – 4**.

Bond type	Bond length / Å			
	1	**2**	**3**	**4**
$Ln^{III}–O_L$	2.237(8)	2.243(4)	2.150(9)	2.145(8)
$Ln^{III}–O_{L–Me}$	2.657(9)	2.648(6)	2.602(5)	2.598(9)
$Ln^{III}–O_{acac}$	2.484(2)–2.492(1)	2.469(0)–2.475(9)	2.369(6)–2.380(1)	2.350(6)–2.364(1)

Table S4. Selected bond lengths for **5** and **6**.

Bond type	Bond length / Å	
	5	**6**
$Ln^{III}–O_L$	2.192(6) and 2.214(6)	2.124(4) and 2.126(9)
$Ln^{III}–O_{L–Me}$	2.585(4) and 2.610(0)	2.529(1) and 2.533(3)
$Ln^{III}–O_{[Mo5]}$	2.524(7)–2.575(1)	2.414(6)–2.458(9)
$Mo^{IV}–O$	1.696(9)–2.364(6)	1.678(7)–2.347(4)
$Mo_{NO}–O$	1.991(4)–2.128(5)	1.991(4)–2.109(0)

II.2. Powder X-ray diffraction

PXRD measurements for **1 – 6** (**Figs. S4–S6**) were performed in a transmission geometry on a thin transparent section using Cu-Kα radiation (λ = 1.54059 Å) and a focusing Ge-monochromator (Johann-type) at room temperature. The exposure time was 1 hour. The PXRD patterns for **1 – 6** fit very well with the theoretical curves calculated from SXRD data, confirming the phase homogeneity of experimental **1 – 6**. The randomly oriented crystallites in the samples may result in some difference in the intensity of experimental and theoretical reflexes. The changes in lattice size at different temperatures (PXRD diffraction was carried out at room temperature while SXRD diffraction was carried out at 100 K) may result in small shifts of reflex positions between the experimental and theoretical values.

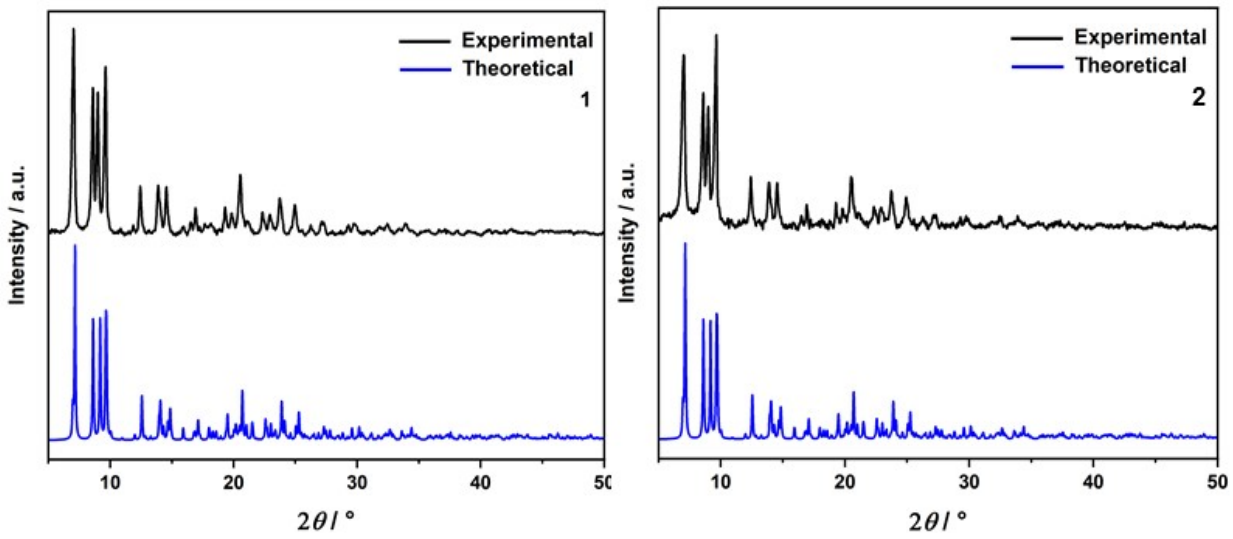

Fig. S5. Experimental pattern (black line) and theoretical curves calculated from single crystal X-ray data (blue line) for **1** and **2**.

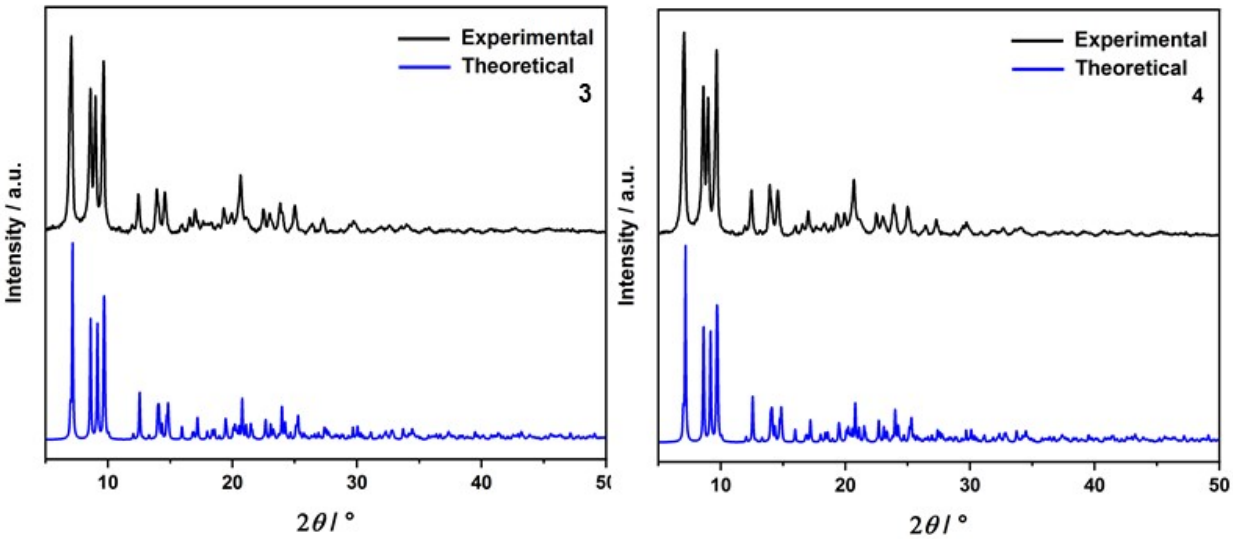

Fig. S6. Experimental pattern (black line) and theoretical curves calculated from single crystal X-ray data (blue line) for **3** and **4**.

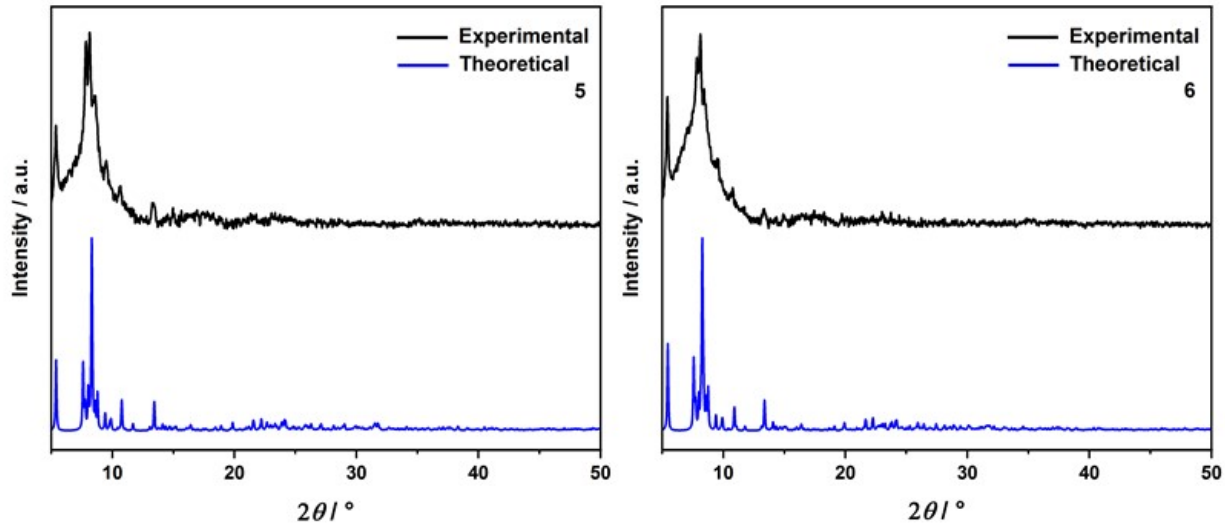

Fig. S7. Experimental pattern (black line) and theoretical curves calculated from single crystal X-ray data (blue line) for **5** and **6**.

III. ESI-HRMS

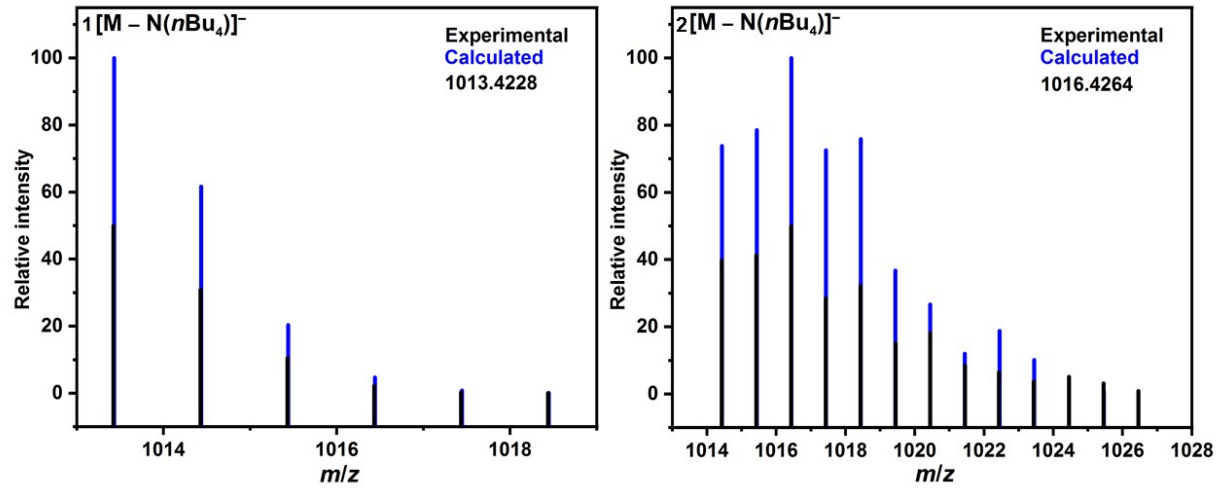

Fig. S8. ESI-HRMS pattern of **1** and **2**. (**Left**) *m/z*, found 1013.4228 $[M - N(nBu_4)]^-$ (100%), calculated for $[C_{56}H_{72}O_8Pr]^-$ 1013.4309. M stands for $(N(nBu)_4)[Pr^{III}L(acac)_2]$. (**Right**) *m/z*, found 1040.4540 $[M - N(nBu_4)]^-$ (100% relative abundance), calculated for $[C_{56}H_{72}O_8Er]^-$ 1040.4572. M stands for $(N(nBu)_4)[Er^{III}L(acac)_2]$. Experimental relative intensity values have been adjusted to 50% for the purpose of comparison.

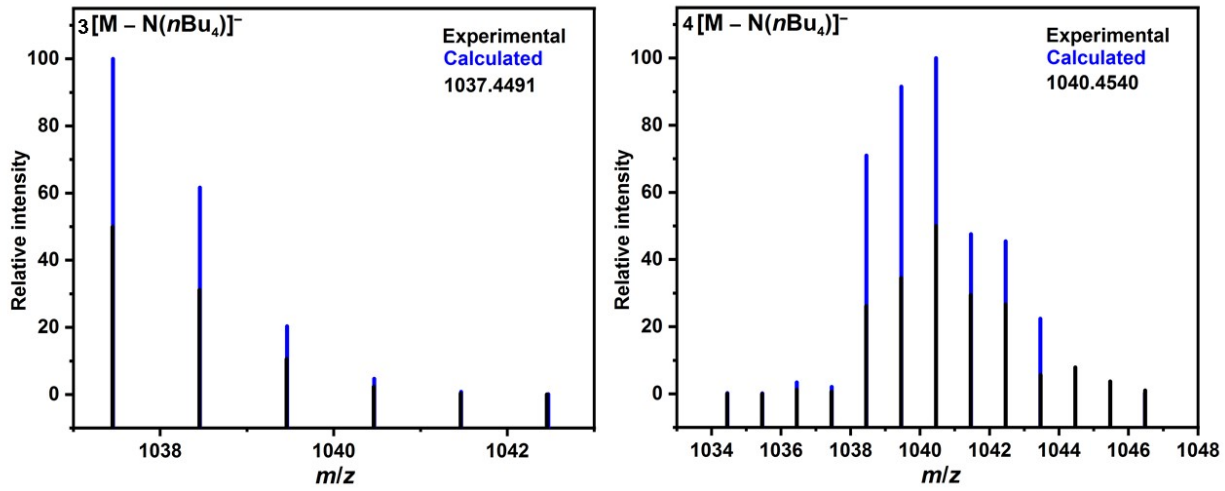

Fig. S9. ESI-HRMS pattern of **3** and **4**. (**Left**) *m/z*, found 1016.4264 $[M - N(nBu_4)]^-$ (100% relative abundance), calculated for $[C_{56}H_{72}O_8Nd]^-$ 1013.4348. M stands for $(N(nBu)_4)[Nd^{III}L(acac)_2]$. (**Right**) *m/z*, found 1037.4491 $[M - N(nBu_4)]^-$ (100%), calculated for $[C_{56}H_{72}O_8Ho]^-$ 1037.4536. M stands for $(N(nBu)_4)[Ho^{III}L(acac)_2]$. Experimental relative intensity values have been adjusted to 50% for the purpose of comparison.

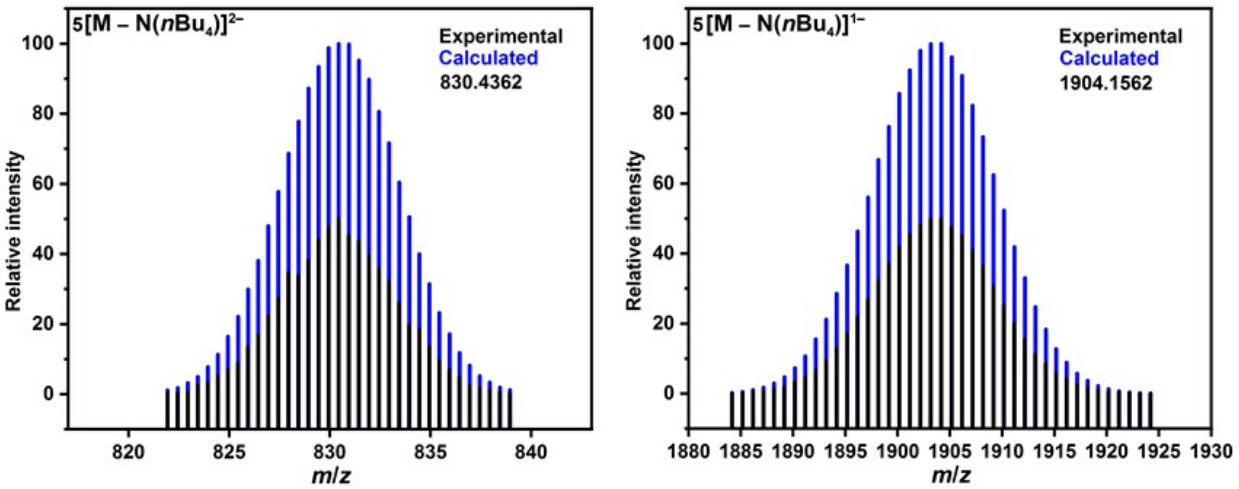

Fig. S10. ESI-HRMS pattern of **5**. (**Left**) *m/z*, found 830.4362 $[M - 2\ N(nBu)_4]^{2-}$ (6.15%), calculated for $[C_{50}H_{70}NO_{22}Mo_5Nd]^{2-}$ 830.4408. (**Right**) *m/z*, found 1904.1562 $[M - N(nBu)_4]^{1-}$ (100%), calculated for $[C_{66}H_{106}N_2O_{22}Mo_5Nd]^{1-}$ 1904.1665. M stands for $(N(nBu)_4)_2[Nd^{III}L\{Mo_5O_{13}(OMe)_4(NO)\}]$. Experimental relative intensity values have been adjusted to 50% for the purpose of comparison.

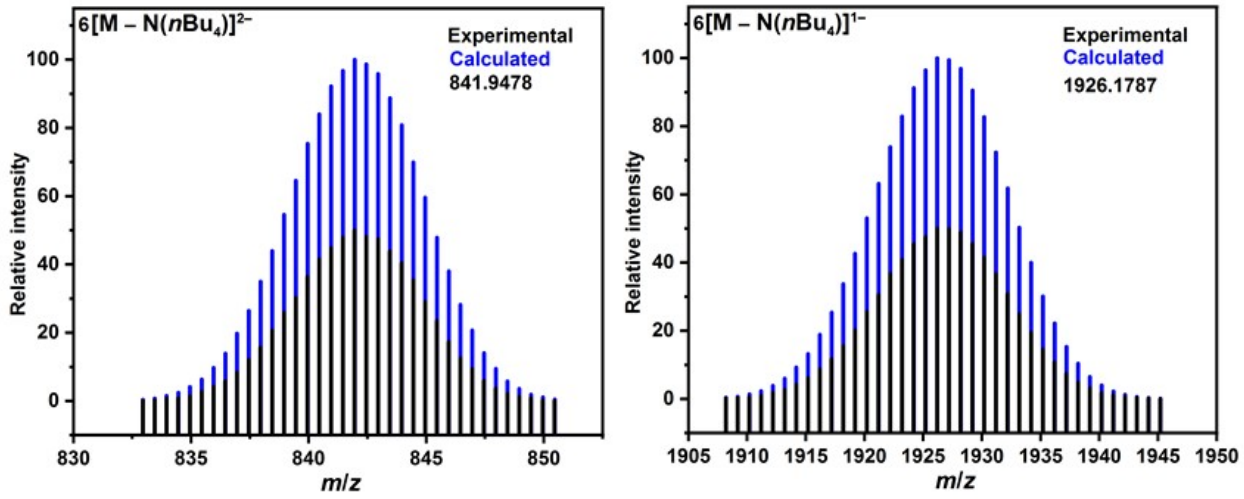

Fig. S11. ESI-HRMS pattern of **6**. (**Left**) *m/z*, found 841.9478 $[M - 2\ N(n\text{Bu})_4]^{2-}$ (100%), calculated for $[C_{50}H_{70}NO_{22}Mo_5Er]^{2-}$ 841.9515. (**Right**) *m/z*, found 1926.1787 $[M - N(n\text{Bu})_4]^{1-}$ (45.78%), calculated for $[C_{66}H_{106}N_2O_{22}Mo_5Er]^{1-}$ 1926.1875. M stands for $(N(nBu)_4)_2[Er^{III}L\{Mo_5O_{13}(OMe)_4(NO)\}]$. Experimental relative intensity values have been adjusted to 50% for the purpose of comparison.

IV. FT-IR spectroscopy

The FT-IR spectra of **1 – 6** and a comparison of starting material are shown on **Figs. S11–S13**. The complexes **1 – 4** and **5 – 6** display similar peaks in the spectra, hence, we provide a representative description for **4** and **6** in comparison with uncoordinated H_2L ligand. They all display medium-intense bands in the range of 2800–3000 cm^{-1} corresponding to the C–H stretching. The bands at 1635, 1482, 1461, and 1363 cm^{-1} in the spectra of H_2L are attributed to aromatic C=C bending vibrations.

They are slightly shifted after coordination with Ln^{III}, corresponding to the bands at 1593, 1479, 1462, and 1334 cm^{-1} in the spectra of **4** and at 1621, 1479, 1430, and 1334 cm^{-1} in the spectra of **6**. The strong band appearing at 1509 cm^{-1} in the spectra of **4** is assigned to the C–C=O vibration since it does not appear in **6** and H_2L. One additional band at 1299 cm^{-1} in H_2L, corresponding to that at 1312 cm^{-1} in **4** and 1315 cm^{-1} in **6**, is due to CH_3 bending vibrations. The other two bands observed at 1170 cm^{-1} and the strong band at 1205 cm^{-1} in H_2L belong to C-C bending and C-O stretching vibrations, in comparison with 1170 and 1206 cm^{-1} in **4**, and 1168 and 1212 cm^{-1} in **6**. The very weak bands in the range of 1120–1012 cm^{-1} in the spectra of H_2L, 1126–911 cm^{-1} in **4**, and 1168–927 cm^{-1} in **6**, feature in-plane C-H bending vibrations. Two medium intensity bands at 873 and 800 cm^{-1} in the spectra of H_2L, 872 and 811 cm^{-1} in **4** and 838 and 790 cm^{-1} in **6**, are assigned to out-of-plane C–H bending vibrations. The additional bands at 1315, 927–838, and 680 cm^{-1} in the spectra of **6** feature N–O bending, Mo–O bending, and Mo–O–Mo bending vibrations, confirming the coordination with the $[Mo_5O_{13}(OMe)_4(NO)(MeOH)]^{3-}$ unit.

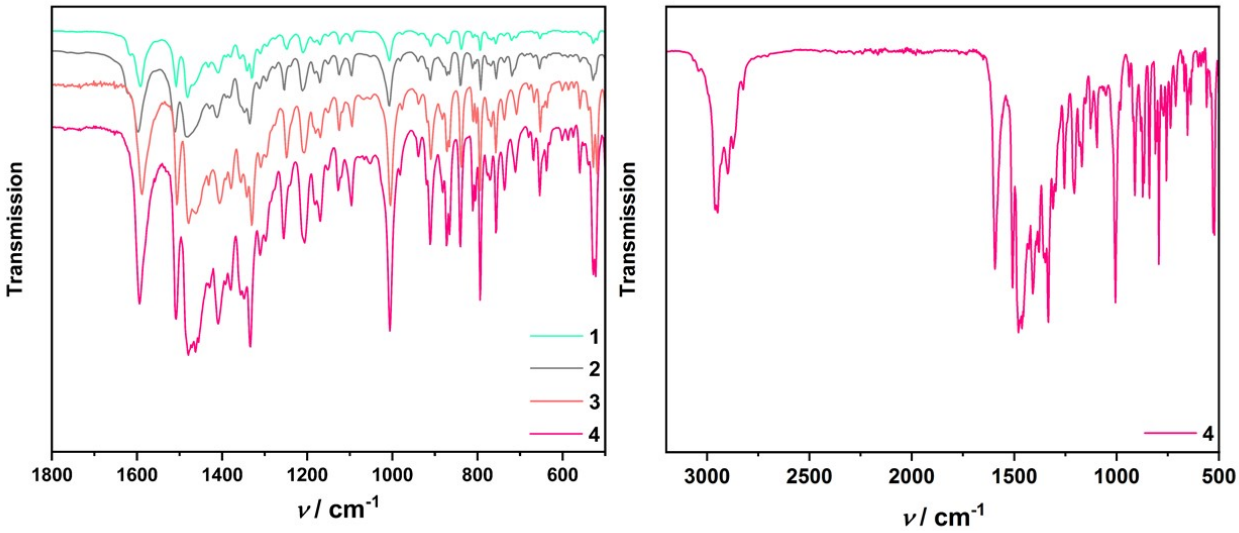

Fig. S12. FT-IR spectra of **1** (green), **2** (gray), **3** (orange), and **4** (pink).

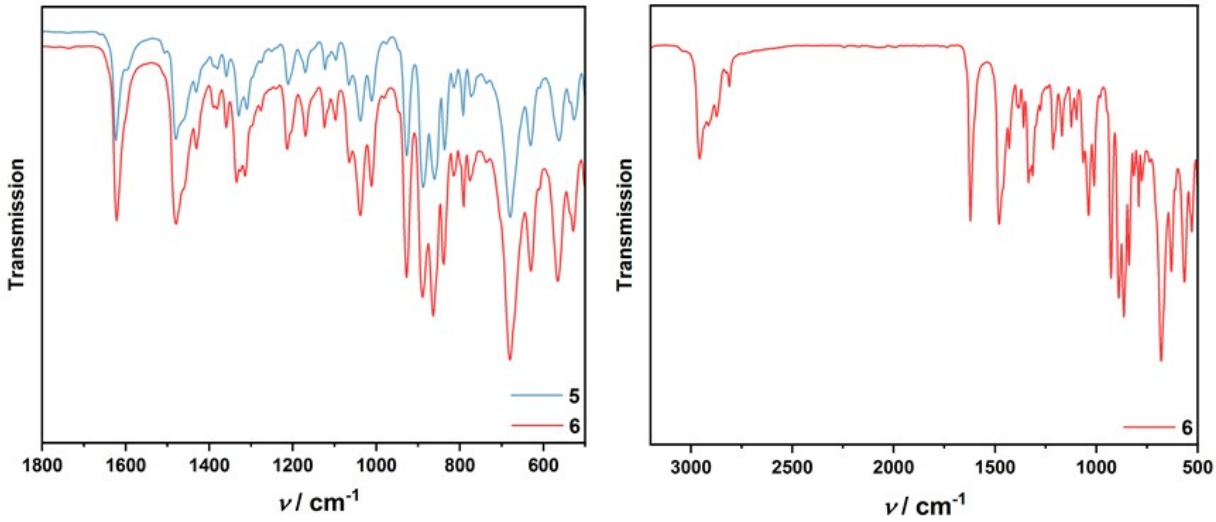

Fig. S13. FT-IR spectra of **5** (blue) and **6** (red).

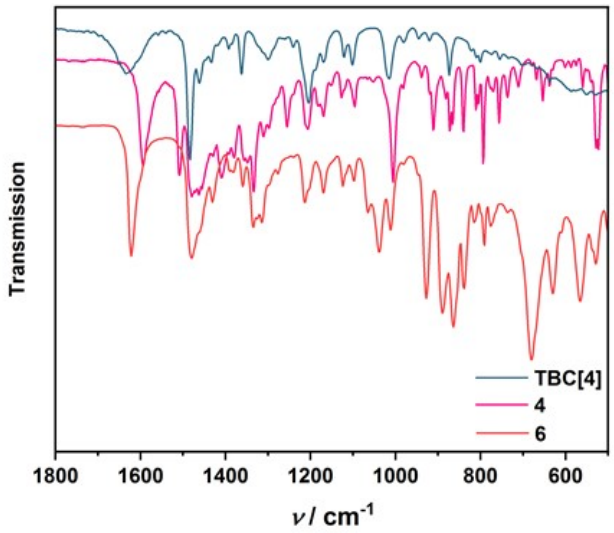

Fig. S14. FT-IR spectra of **4** and **6** in comparison to H_2L (blue).

V. Thermogravimetric analysis

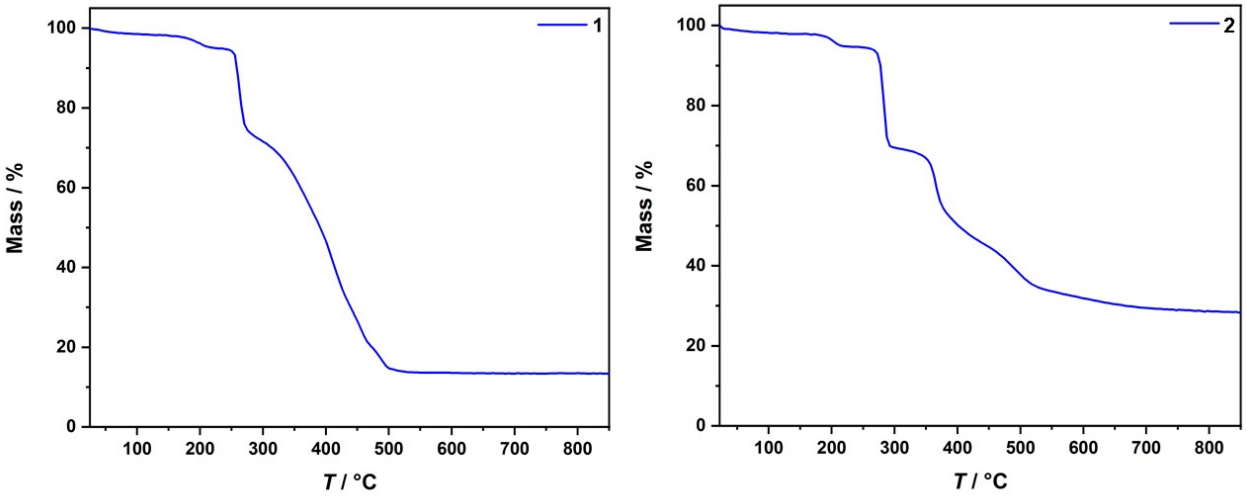

Fig. S15. TGA curves for **1** and **2** from room temperature to 950 °C.

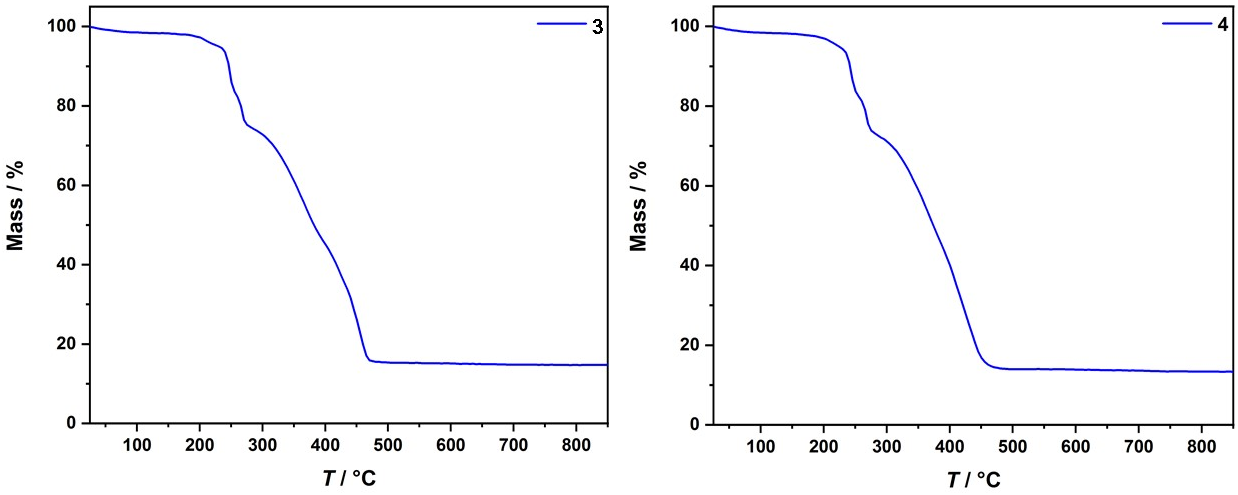

Fig. S16. TGA curves for **3** and **4** from room temperature to 950 °C.

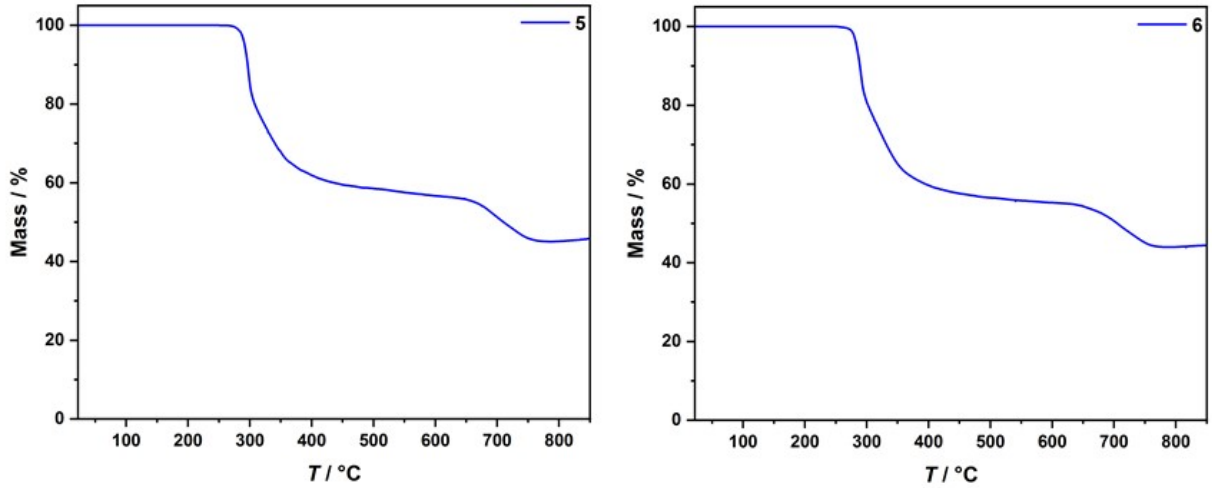

Fig. S17. TGA curves for **5** and **6** from room temperature to 950 °C.

VI. UV-Vis spectroscopy

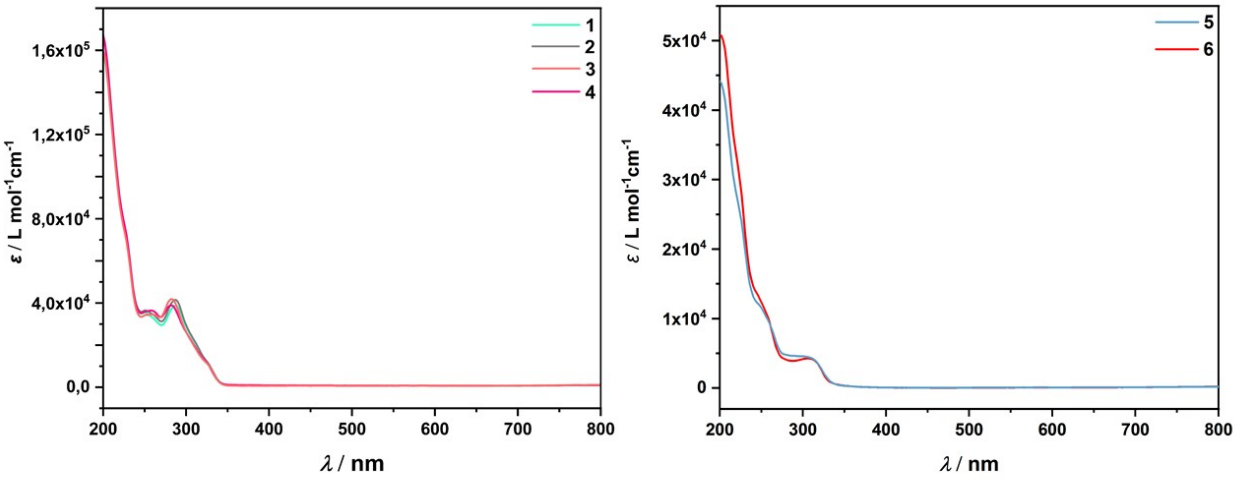

Fig. S18. UV-Vis curves of **1** – **4** (left) and **5** and **6** (right).

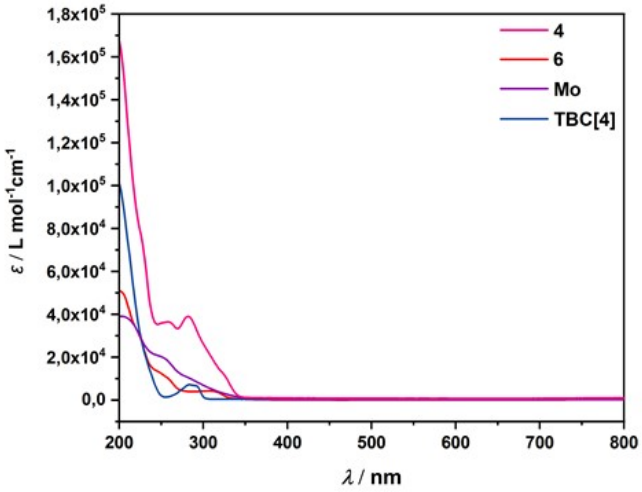

Fig. S19. UV-Vis curves of **4** and **6** in comparison to H_2L (navy) and {Mo_5} (purple).

VII. Magnetic study

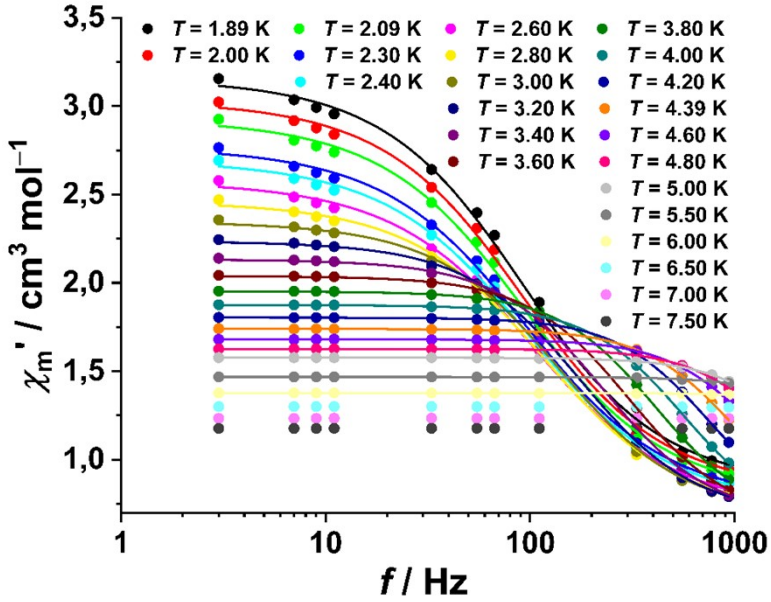

Fig. S20. The χ_m' vs. frequency f plot of **4** at a static magnetic bias field of 300 Oe. Symbols: data, lines: fit to generalized Debye expression.

Although we observed out-of-phase signals with significant magnitude for **6**, the curvature in the Cole-Cole plot is very small or, alternatively, no maxima in the χ_m'' vs. f plots are observed (Fig. S20a and c) within the probed parameter range. Therefore, the following analysis should be taken with care. The relaxation times τ at each temperature (Fig. S20d) were extracted from the data by simultaneously fitting the χ_m' vs. f and χ_m'' vs. f data with a generalized Debye expression[5] (Fig. S20b and c). The distribution of these relaxation times $\alpha = 0.150 \pm 0.020$ suggests multiple relaxation pathways. However, due to the large error margins, we assumed only a single dominant relaxation process in the observed temperature range. The best fit to the τ vs. $1/T$ data could be achieved by assuming an Orbach slow relaxation process. The equation $\tau^{-1} = \tau_0^{-1} \times \exp(-U_{eff}/(k_B T))$ with the attempt time τ_0, the effective energy barrier U_{eff} and the Boltzmann constant k_B represents such a relaxation process. The least-squares fits yields $\tau_0 = (1.0 \pm 0.6) \times 10^{-7}$ s and $U_{eff} = (7.7 \pm 0.8)$ cm^{-1}. Such values are very common for single-ion lanthanide SMMs.[6] Regarding the data of the Nd^{3+} compounds: After correcting the data, the χ_m'' values are very small. Considering the rather large corrections, we assume that these signals are predominantly due to impurities.

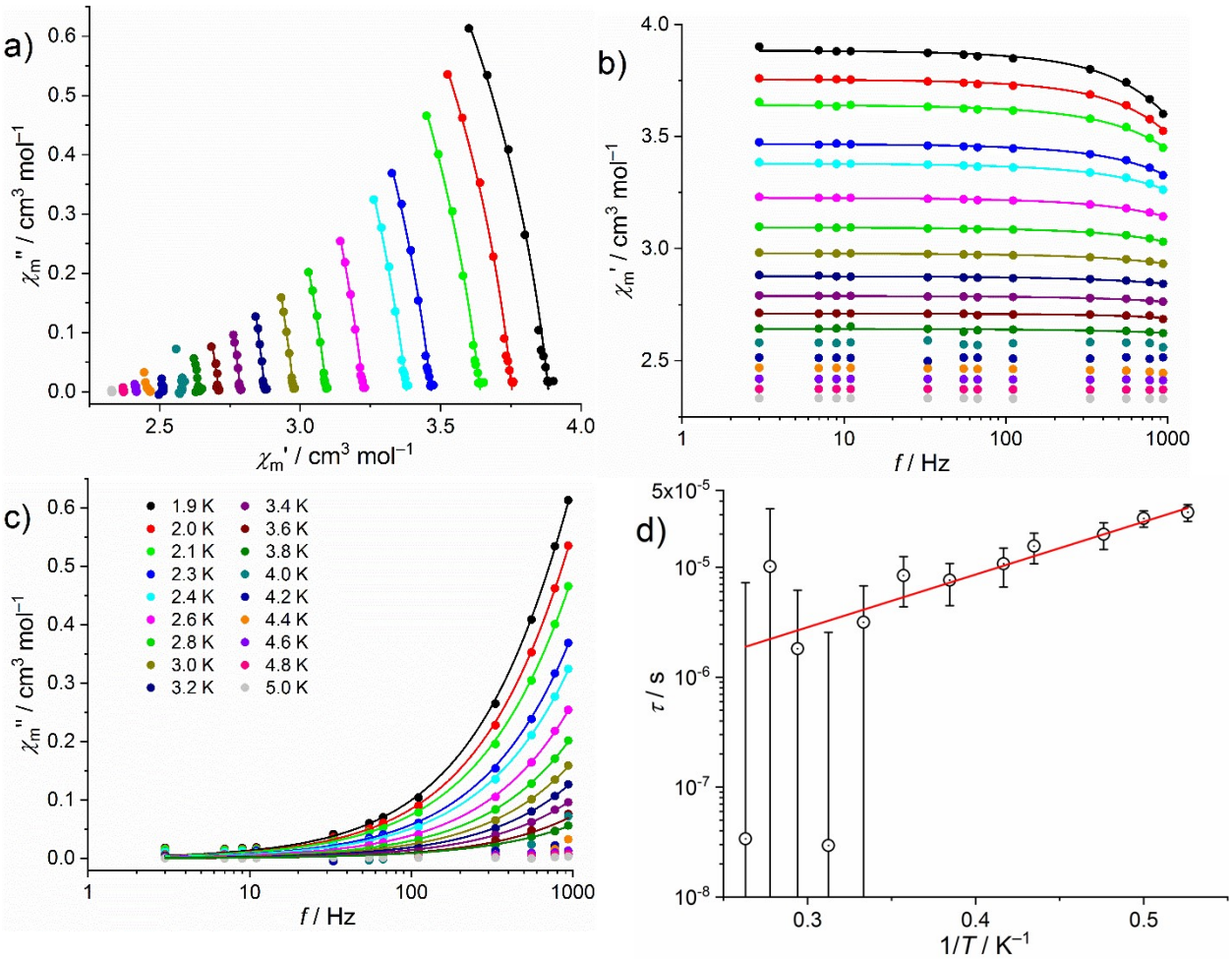

Fig. S21. Magnetic ac measurements of **6** at a static magnetic bias field of 300 Oe: (a) Cole-Cole plot of out-of-phase χ_m'' vs. in-phase molar magnetic susceptibility χ_m', (b) χ_m' vs. frequency f plot, (c) χ_m'' vs. f plot, (d) relaxation times τ vs. inverse temperature $1/T$ plot (for T = 1.9 – 3.8 K). Symbols in (a)–(c): data, lines: fit of the generalized Debye expression to the in-phase and out-of-phase susceptibility data. Color code: see legend in (c), solid red line in (d): fit to an Orbach slow relaxation process.

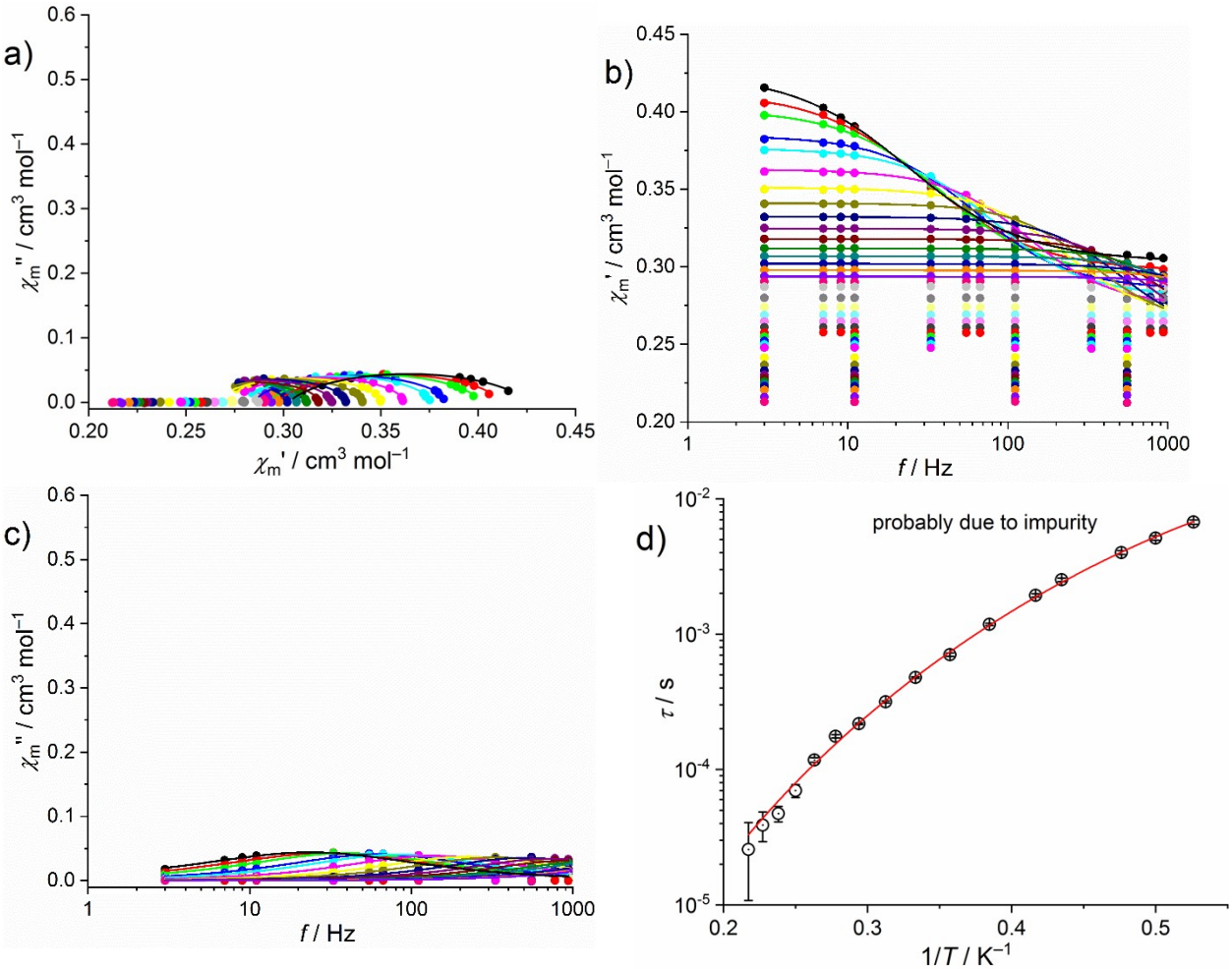

Fig. S22. Magnetic ac measurements of **2** at a static magnetic bias field of 300 Oe. The out-of-phase effects are, at least partially, assigned to an impurity as their magnitude fluctuates in between separately synthesized batches.

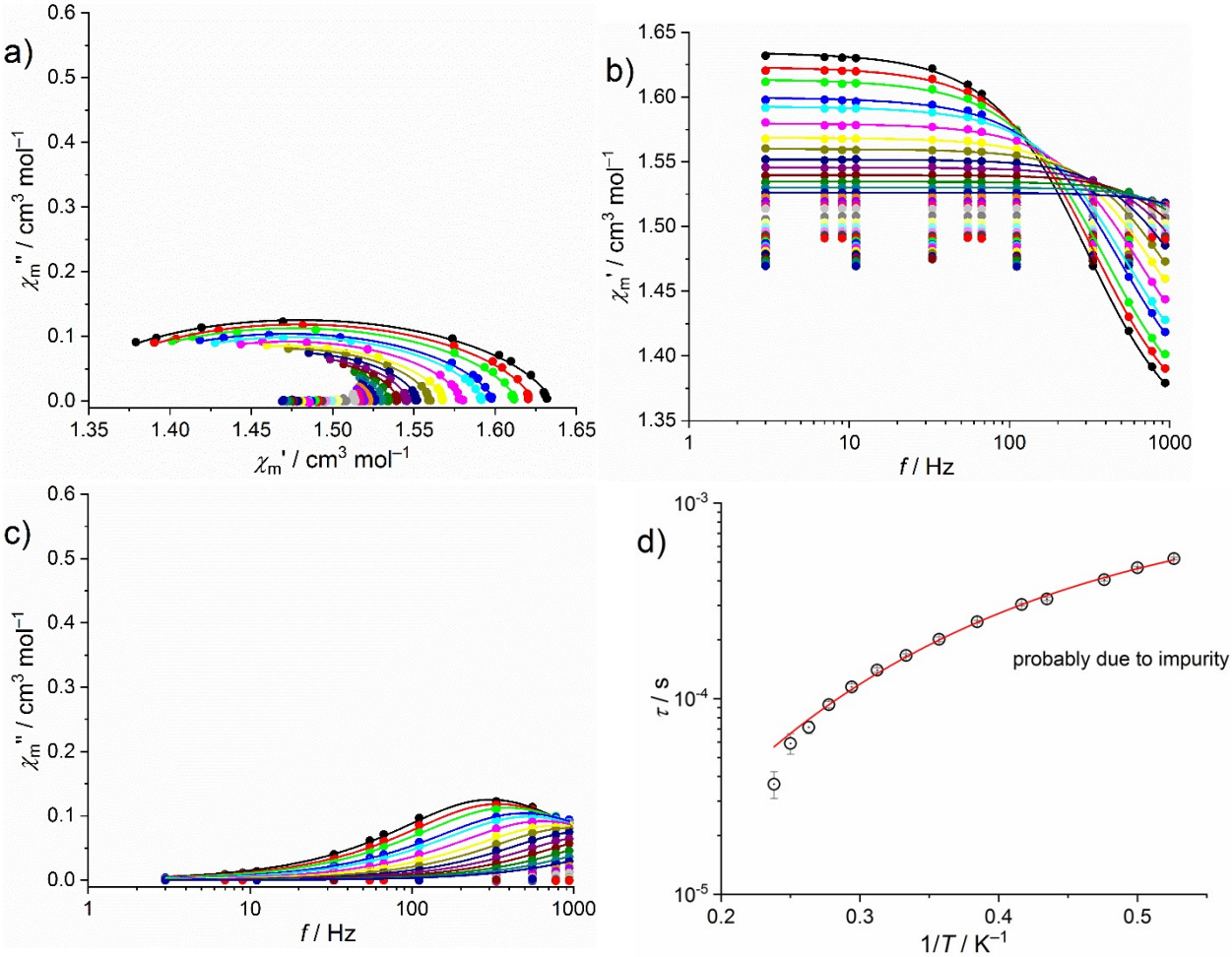

Fig. S23. Magnetic ac measurements of **5** at a static magnetic bias field of 300 Oe. The out-of-phase effects are, at least partially, assigned to an impurity as their magnitude fluctuates in between separately synthesized batches.

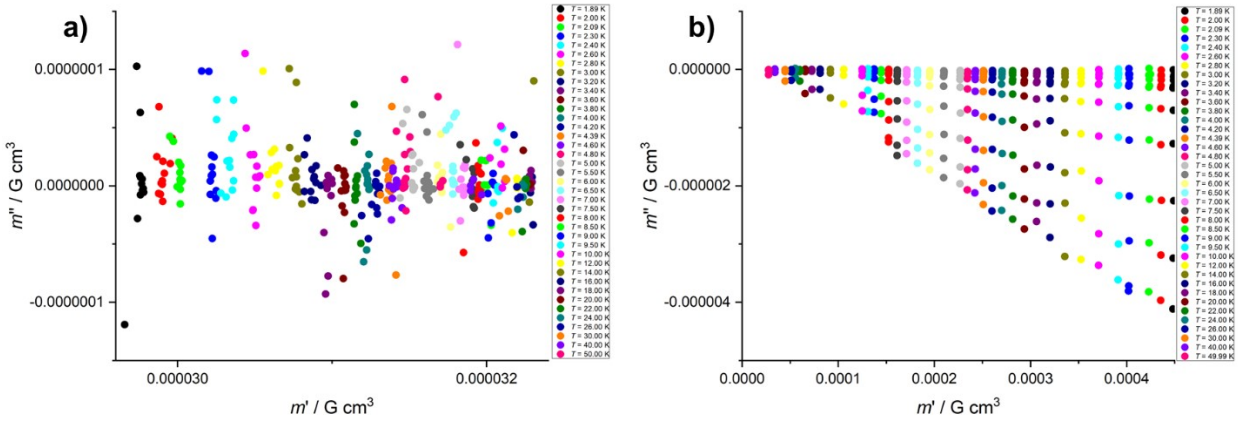

Fig. S24. Magnetic ac measurements of **1** (a) and **3** (b) at a static magnetic bias field of 300 Oe.

VIII. Electrochemical study

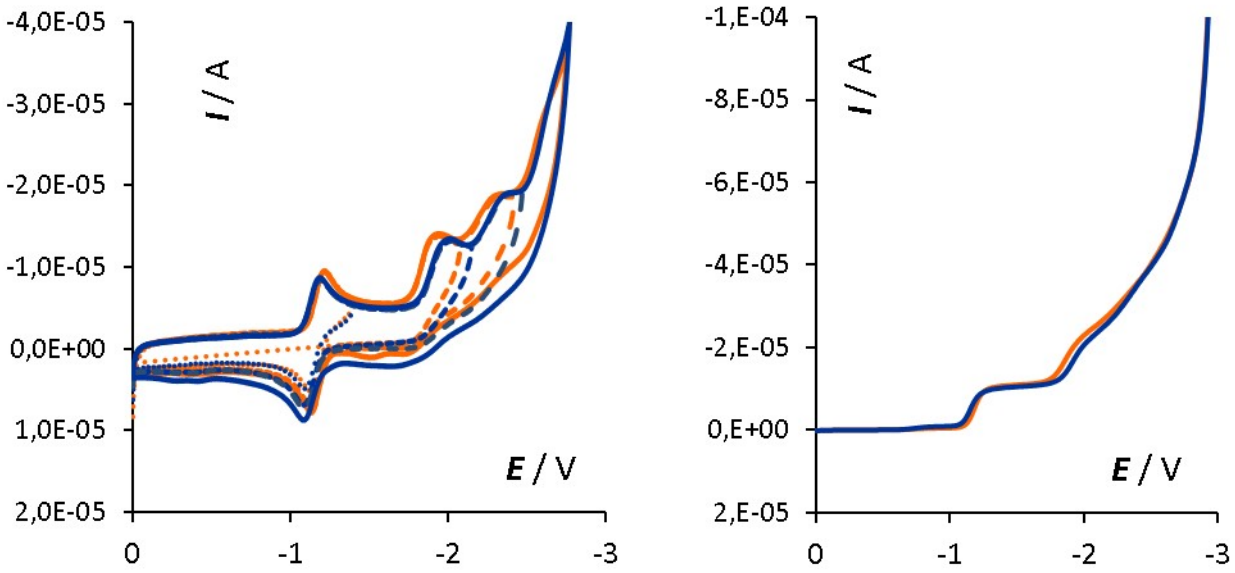

Fig. S25. Cyclic voltammograms (left; 200 mV s^{-1}) and RD-voltammograms (right; 1000 rpm) of reduction of compounds **5** (orange) and **6** (blue). GC electrodes, DMF.

Table S5. Oxidation and reduction potentials of **1** – **6** (conc. 5 x 10^{-4} mol/L), taken from cyclic voltammetry (GC stationary disk electrode, 200 mV s^{-1}) and rotating disk voltammetry (GC, 1000 rpm) in DMF.

	$E^0_{ox}(2)$[a] V, vs. SCE	$E^0_{ox}(1)$[a] V, vs. SCE	$E^0_{red}(1)$[a] V, vs. SCE	$E_{pc,red}(2)$[b] V, vs. SCE	$E_{pc,red}(3)$[b] V, vs. SCE	$E_{pc,red}(4)$[b] V, vs. SCE
1	0.53 (0.58)[d]	0.33 (0.33)[d]	-[c]	-[c]	-[c]	
2	0.54 (0.59)[d]	0.34 (0.34)[d]	-[c]	-[c]	-[c]	
3	0.59 (0.63)[d]	0.33 (0.34)[d]	-[c]	-[c]	-[c]	
4	0.60 (0.63)[d]	0.33 (0.33)[d]	-[c]	-[c]	-[c]	
5	0.76 (0.78)[d]	0.53 (0.54)[d]	–1.18 (–1.18)[d]	–1.93 (–1.86)[d]	–2.30 (–2.3)[d]	–2.6[e]
6	0.79 (0.80)[d]	0.53 (0.53)[d]	–1.14 (–1.15)[d]	–1.99 (–1.89)[d]	–2.37 (–2.3)[d]	–2.7[e]

[a] E^0: standard redox potential as the mean value of the anodic and cathodic peak potentials $(E_{pa} + E_{pc})/2$
[b] Cathodic (anodic) peak potential in case of irreversible redox step
[c] No reduction up to –2.8 V
[d] In brackets – data as $E_{1/2}$ taken from the GC-RDE voltammetry, (1000 rpm, 10 mV s^{-1})
[e] Indistinctive shoulder

References

1. STOE X-Red32, absorption correction by Gaussian integration, analogous to P. Coppens, The Evaluation of Absorption and Extinction in Single-Crystal Structure Analysis. Crystallographic Computing (Ed.: F. R. Ahmed), Munksgaard, Copenhagen, 1970, pp. 255–270.
2. J. Koziskova, F. Hahn, J. Richter and J. Kozisek, *Acta Chim. Slov.*, 2016, **9**, 136.
3. G. M. Sheldrick, *Acta Crystallogr.*, 2015, **C71**, 3.
4. M. Llunell, D. Casanova, J. Cirera, P. Alemany, S. Alvarez, SHAPE 2.1, Universitat de Barcelona, 2013.
5. K. S. Cole and R. H. Cole, *J. Chem. Phys.*, 1941, **10**, 98–105.
6. D.N. Woodruff, R.E.P. Winpenny, R.A. Layfield, *Chem. Rev.*, 2013, **113**, 5110–5148.